In Situ Construction of Uniform and Robust Cathode-electrolyte Interphase for Li-rich Layered Oxides

Jingteng Zhao, Yuan Liang, Xu Zhang, Zihe Zhang, Errui Wang, Shiman He, Boya Wang, Zhijie Han, Jun Lu, Khalil Amine, and Haijun Yu**

J. Zhao, Dr. Y. Liang, Prof. X. Zhang, Dr. Z. Zhang, E. Wang, Dr. S. He, B. Wang, Z. Han, Prof. H. Yu
Faculty of Materials and Manufacturing
Beijing University of Technology
Beijing, 100124, China
E-mail: hj-yu@bjut.edu.cn

Prof. J. Lu, Prof. K. Amine
Chemical Sciences and Engineering Division
Argonne National Laboratory
Argonne, Illinois 60439, USA
E-mail: amine@anl.gov

Prof. K. Amine
Material Science and Engineering
Stanford University
Stanford, CA 94305, USA

Prof. K. Amine
Institute for Research and Medical Consultations
Imam Abdulrahman Bin Faisal University
Dammam 34212, Saudi Arabia

Keywords: in situ contruction, cathode-electrolyte interphase, li-rich layered oxides, voltage decay, lithium-ion battery

The high-energy-density Li-rich layered oxides (LLOs) as promising cathodes for Li-ion batteries suffer from the dissolution of transition metals (especially manganese) and severe side reactions in conventional electrolytes, which greatly deteriorate their electrochemical performance. Herein, an *in situ* "anchoring + pouring" synergistic cathode-electrolyte interphase (CEI) construction is realized by using 1,3,6-hexanetricarbonitrile (HTCN) and tris(trimethylsilyl) phosphate (TMSP) electrolyte additives to alleviate the challenges of an LLO ($Li_{1.13}Mn_{0.517}Ni_{0.256}Co_{0.097}O_2$). HTCN with three nitrile groups can tightly anchor

transition metals by coordinative interaction to form the CEI framework, and TMSP will electrochemically decompose to reshape the CEI layer. The uniform and robust *in situ* constructed CEI layer can suppress the transition metal dissolution, shield the cathode against diverse side reactions, and significantly improve the overall electrochemical performance of the cathode with a discharge voltage decay of only 0.5 mV/cycle. Further investigations based on a series of experimental techniques and theoretical calculations have revealed the composition of *in situ* constructed CEI layers and their distribution, including the enhanced HTCN anchoring effect after lattice densification of LLOs. This study provides insights into the *in situ* CEI construction for enhancing the performance of high-energy and high-voltage cathode materials through effective, convenient and economical electrolyte approaches.

1. Introduction

The expanding application of lithium-ion batteries (LIBs) in portable electronics, electric vehicles, and other technologies calls for the rapid progress of high-energy-density cathode materials.[1-5] Among various candidates, Li-rich layered oxides (LLOs) have gained great attentions owing to their high energy densities of ~ 1000 Wh kg^{-1}.[6,7] However, LLOs suffer from rapid capacity fading, sluggish kinetics and severe voltage decay, which are largely associated with the irreversible surface structural transitions.[8,9] In particular, the anionic redox of lattice O in LLOs can be triggered at high voltage, leading to the release of active O species into the electrolyte.[10] This process severely aggravates the irreversible structural transitions and arises various interfacial side reactions associated with the electrolyte decomposition and transition metal (TM) dissolution.[11,12] Furthermore, a cathode-electrolyte interphase (CEI) layer can be formed, which may retard the Li^+ diffusions and reduce the electrochemical efficiency of LLOs if not well regulated.[13,14]

The electrochemical stability of LLOs can be enhanced by modifying their surface structure, either by pre-coating or *in situ* construction.[15-18] The pre-coating with a protective layer is effective to attenuate the irreversible structural transitions, while the *in situ* construction of a well-defined CEI layer during electrochemical reactions provides a more convenient route with similar or even better effects.[19,20] However, compared with conventional cathodes, LLOs raise more rigid physical and chemical requirements for a beneficial CEI layer owing to their specific anionic redox and surface structure evolution.[21] On the one hand, the CEI layer should be compact and continuous to separate the cathode from electrolyte contact to effectively suppress side reactions.[22] A balance between robustness and flexibility for the CEI layer is also important to stably tolerate the electrochemical volume changes of LLOs.[23] Moreover, the ultrathin and ultra uniform morphology of CEI layer is critical to favor the fast Li^+ diffusion.[24] These physical properties can only be realized by elegant (electro)chemical design. On the other hand, the chemical functional groups confined in the CEI layer should be well chosen to promote the Li^+ diffusion as well as to deliver multiple functions such as strengthening layer robustness, avoiding electrolyte penetration, locking TM ions from dissolution, and so on.[25-27] These functional groups should be relatively chemically/electrochemically stable, which can consistently take effect upon long cycles.[28] Moreover, an intimate contact between the CEI and the dynamic LLOs surface is necessary to enhance the structure compatibility, which requires strong chemical interactions between LLO surface and CEI components.[29] Toward these complicated goals, rational CEI design strategies based on the synergy of functions are urgently required.

To realize the above goals in CEI construction, it is also critical to consider the LLO structures intrinsically and dynamically. As shown in our previous studies on the structural identification and evolution of LLOs, in the initial cycle, LLOs will transform from a “twin domain” structure (rhombohedral $LiTMO_2$ and monoclinic Li_2MnO_3, where TM=transition metal) into a “core-

shell" structure (the core is a monoclinic $LiTMO_2$-like structure core, and the shell consists of rock salt TMO and spinel TM_3O_4 structures).[7,30,31] During this evolution, TM (predominantly Mn) dissolution, irreversible oxygen release, solvent oxidation, and $LiPF_6$ decomposition, as well as many other side reactions, also take place particularly at high voltages, significantly deteriorating the LLO structure and electrochemical reversibility.[9-11] These side reactions can be partially addressed by the bulk gradient design or the surface nanocomposite construction to gain better performance.[32,33] Still, a CEI structure with consistent or even strengthened stabilization effects during the electrochemical cycling is highly beneficial.

Inspired by the ferroconcrete construction for buildings, we proposed here an "anchoring + pouring" strategy to *in situ* fabricate a uniform and robust CEI structure for LLOs. A relatively rigid molecule with fine chemical/electrochemical stability, appropriate size, and strongly coordinative groups tightly anchors the LLO surface to serve as the CEI framework, while an electrochemically decomposable molecule provides mobile moieties to participate in the *in situ* "pouring" within the CEI framework. Such a strategy could produce a CEI layer with excellent compactness and integrity, balanced robustness and flexibility, and ultrathin thickness. Moreover, by elegant controlling the CEI compositions from appropriate electrolyte additives, the CEI layer could possess high Li^+ conductivity and multiple functions, high chemical/electrochemical stability, and intimate contact with LLOs. Among numerous candidates for this strategy, the nitrile-based molecule is a promising CEI framework unit for its high-voltage stability, Li^+ penetration permissibility, high polarity, low flammability, and strong coordination with TMs.[34-38] On the other hand, the (Si-O)-containing molecules can preferentially decompose to facilitate the *in situ* "pouring" of various fragments to form a cross-linked flexible CEI layer.[39,40] Subsequently, the "anchoring + pouring" synergy in CEI construction significantly enhance the electrochemical stability of LLOs, by suppressing the irreversible side reactions and TM dissolutions. The effectiveness and mechanism of this CEI

strategy is well demonstrated on a representative LLO ($Li_{1.13}Mn_{0.517}Ni_{0.256}Co_{0.097}O_2$) as displayed experimentally and theoretically in below.

2. Result and Discussion

2.1. Synergistic Electrolyte Additive Strategy

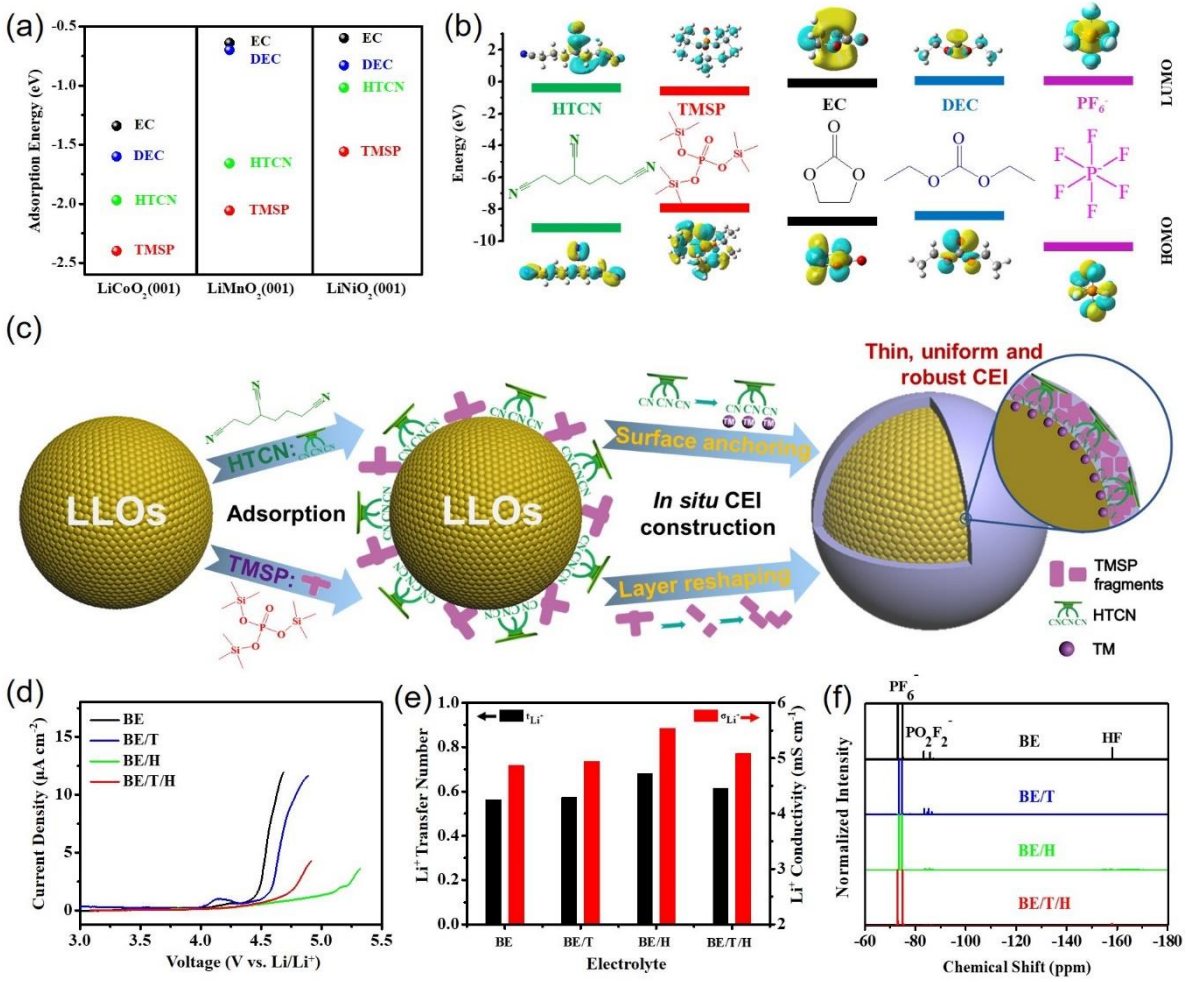

Figure 1. The synergistic HTCN + TMSP electrolyte additives for *in situ* CEI construction of LLOs. a) Calculated adsorption energies of EC, DEC, HTCN, and TMSP on the (001) surfaces of the model cathodes $LiCoO_2$, $LiMnO_2$ and $LiNiO_2$. b) Calculated HOMOs and LUMOs of HTCN, TMSP, EC, DEC and PF_6^-. c) Schematic illustration of the synergistic effects of HTCN + TMSP on adjusting the CEI structure and cathode electrochemistry. d) LSV profiles of BE, BE/T, BE/H and BE/T/H electrolytes at a scan rate of 0.1 mV s^{-1}. e) Li^+ transfer number and Li^+ conductivity of the four electrolytes at 25 °C. f) ^{19}F NMR spectra of the four electrolytes after adding 1000 ppm H_2O. The spectra were normalized according to the PF_6^- peak at −72 ppm.

To *in situ* construct the CEI layer for LLOs protection, two additives including 1,3,6-hexanetricarbonitrile (HTCN) and tris(trimethylsilyl) phosphate (TMSP) have been coupled to modify the commercial electrolyte $LiPF_6$ in EC/DEC (1/1 by volume). HTCN has three electron-rich nitrile groups (-CN) to anchor the TM as CEI framework,[41] while TMSP undergoes electrochemical decomposition to *in situ* pour the CEI layer.[42] The adsorption priorities of electrolyte components including HTCN, TMSP, EC, and DEC onto the LLO were first estimated according to their adsorption energies on model $LiCoO_2$ (001), $LiMnO_2$ (001) and $LiNiO_2$ (001) surfaces by density functional theory (DFT) calculation. The three model cathodes were chosen for calculation because their layered structures are similar to that of LLOs, while the (001) surface was adopted because of its preferential exposure. As shown in **Figure 1**a, the absolute adsorption energies of the four molecules on all surfaces follow the same sequence of TMSP > HTCN > DEC > EC (note that the coordinative energy between HTCN and TMs is not involved here, as will be discussed below). These findings suggest that HTCN and TMSP additives can adsorb on the LLO surface more readily than EC and DEC solvents, promoting their participation in the construction of the CEI structure.

To further reveal the chemical properties of electrolyte components, the energy levels of HTCN, TMSP, EC, DEC and PF_6^- have been calculated by DFT based on the molecular orbital theory (see computation methods). As displayed in Figure 1b, the highest occupied molecular orbitals (HOMOs) of HTCN, TMSP, EC, DEC, and PF_6^- are −9.08, −7.94, −8.75, −8.41, and −10.12 eV, respectively, indicating the electrochemical stability of HTCN and the highest oxidation priority of TMSP. HTCN has three -CN groups with lone-pair electrons to coordinate with TM atoms, and therefore can anchor surface TM atoms even at high voltages as a stable CEI framework. On the other hand, it is known that a CEI layer can be formed because of the complicated chemical/electrochemical reactions at the cathode surface, and its composition is largely determined by surface adsorption/reaction moieties.[24] Therefore, the preferential

oxidative decomposition of TMSP will provide various moieties to participate in the *in situ* pouring of the CEI layer within the HTCN framework. In addition, the lowest unoccupied molecular orbitals (LUMOs) of HTCN, TMSP, EC, DEC, and PF_6^- are similar to each other, suggesting that the influence of the additives on the anode electrochemistry might be slight.

On the basis of the above investigation, we propose HTCN + TMSP as binary additives for the commercial electrolyte $LiPF_6$ in EC/DEC; they will act synergistically to construct the CEI layer and suppress TM dissolution and irreversible side reactions, as shown in Figure 1c. Both HTCN and TMSP preferentially adsorb on the cathode to prevent the LLO from direct electrolyte contact. During the charge/discharge process, HTCN can tightly anchor the LLO surface by its three -CN functional groups to suppress TM dissolution, widen the electrochemical window of the electrolyte owing to its high oxidation resistance, and serve as a good Li^+ conductor because of its -CN groups.[43] On the other hand, the preferential oxidative decomposition of TMSP predominantly induces the *in situ* formation of a stable CEI layer to shield the cathode against TM diffusion, surface degradation, and electrolyte decomposition. Collectively, the combination of HTCN and TMSP acts to optimize the electrolyte/LLO system, and thus favors high-voltage electrochemistry, inhibits severe TM dissolution, and suppresses harmful side reactions.

According to the proposed synergistic strategy, four electrolytes—1 M $LiPF_6$ in EC/DEC (baseline electrolyte, BE), BE with 1 wt. % TMSP (BE/T), BE with 1 wt. % HTCN (BE/H), and BE with 0.5 wt. % TMSP + 0.5 wt. % HTCN (BE/T/H)—were studied, with a focus on the CEI construction and its effect. The effect of additives on the electrochemical window of electrolytes was first evaluated by linear sweep voltammetry (LSV). As shown in Figure 1d, compared to BE, with an onset oxidation potential of 4.3 V *vs* Li/Li^+ (defined by a current density of 0.7 μA cm^{-2}), BE/T has a small TMSP oxidation peak at 4.15 V, and a sharp current increase at around 4.5 V. In contrast, BE/H shows a higher onset oxidation potential at around

4.6 V, with a sharp current increase at around 5.2 V, suggesting that HTCN can significantly widen the electrochemical window. Owing to the presence of both HTCN and TMSP, BE/T/H shows an onset oxidation potential of 4.53 V, with a sharp current increase at around 4.75 V, indicating its high-voltage tolerance.

The transfer number and ion conductivity reflect the transfer capability of Li^+, and have been examined for the four electrolytes as shown in Figure 1e (detailed methods are given in Figure S1 and Table S1, Supporting Information). Clearly, both the transfer number and conductivity of BE/H are larger than those of BE and BE/T, suggesting that HTCN can efficiently promote Li^+ migration, which could be attributed to the promotion of Li^+ permeation at the -CN site to favor a higher Li^+ mobility.[43] However, BE/H lacks the preferential oxidation sacrificer to construct a perfect CEI protective layer. Therefore, BE/T/H, with the second largest Li^+ transfer number and conductivity, is more advantageous owing to its more balanced properties.

To further investigate the capabilities of HTCN and TMSP for depleting the corrosive F-containing moieties, particularly HF, the four electrolytes were analyzed by ^{19}F nuclear magnetic resonance (NMR) spectroscopy after the addition of 1000 ppm H_2O. In Figure 1f, the strong NMR peaks at −72 and −75 ppm correspond to PF_6^-, the peak at −158 ppm is attributed to HF,[42] and the peaks at −83 and −86 ppm correspond to $PO_2F_2^-$.[44] The corrosive HF as well as $PO_2F_2^-$ are formed from the hydrolytic decomposition of $LiPF_6$.[45] HTCN can consume the trace H_2O in the electrolyte to avoid PF_6^- hydrolysis, while TMSP can reduce HF from the PF_6^- hydrolysis by the strong nucleophilic substitution of -Si-O groups by F^- ions.[42] After the addition of HTCN, TMSP, and HTCN + TMSP, HF as well as $PO_2F_2^-$ has been eliminated, suggesting that HTCN and TMSP are able to synergistically suppress the HF corrosion on LLOs.[41,42]

2.2. Electrochemical Performance

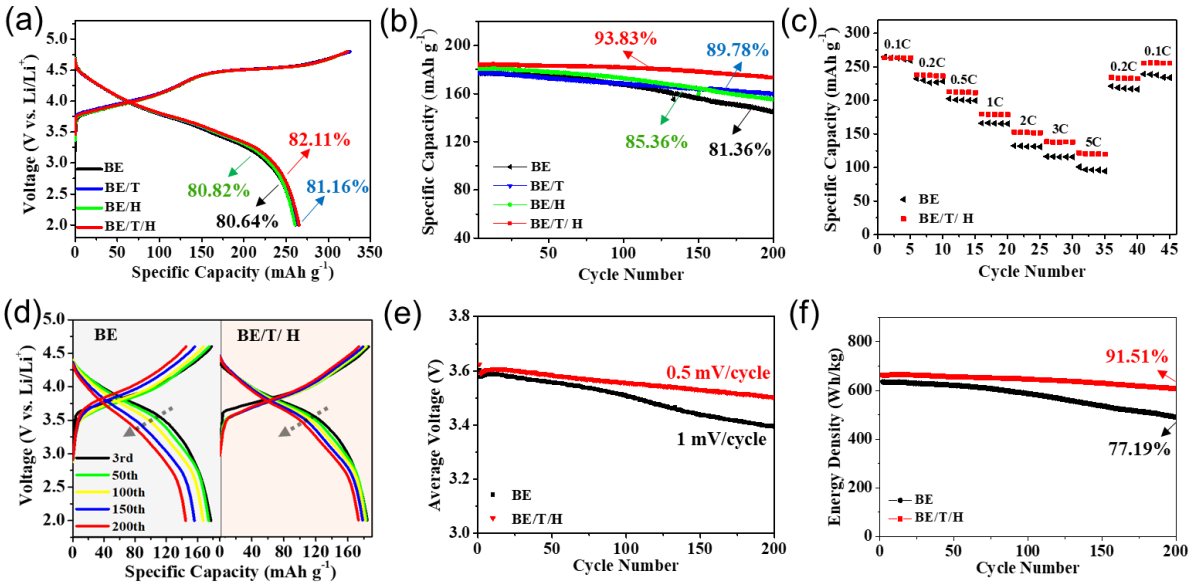

Figure 2. The impacts of HTCN and TMSP on the electrochemical performance of $Li_{1.13}Mn_{0.517}Ni_{0.256}Co_{0.097}O_2$|Li half-cells at 25 °C. a) Initial charge-discharge curves at 0.1 C (1 C = 200 mA g^{-1}). b) Cycle performance at 1 C. c) Rate capability. d) Representative charge-discharge curves from representative cycles. e) Evolution of discharge voltages at 1 C. f) Evolution of energy densities at 1 C.

The impacts of the synergistic HTCN + TMSP additives on the electrochemical performance were evaluated in $Li_{1.13}Mn_{0.517}Ni_{0.256}Co_{0.097}O_2$|Li half-cells between 2.0 and 4.6 V (after the first-cycle activation between 2.0 and 4.8 V). The initial charge-discharge curves of half-cells using the four electrolytes at a current rate of 0.1 C are depicted in **Figure 2**a. The BE/T/H-based cell delivers the highest initial discharge capacity (265.3 mAh g^{-1}) and Coulombic efficiency (82.11%) among the four electrolytes. The cycle performance tests at 1 C (Figure 2b) demonstrate that BE/T/H leads to the best cycle performance, with a capacity retention of 93.83% after 200 cycles, in sharp contrast to BE (81.36%), BE/T (89.78%) and BE/H (85.36%), highlighting the advantages of combined HTCN + TMSP additives for regulating the CEI construction with enhanced cycling stability.

Moreover, as shown in Figure 2c, the BE/T/H-based cell possesses capacities of 263.5 mAh g^{-1} at 0.1 C and 120.2 mAh g^{-1} at 5 C, indicating a smaller capacity drop of 54.4% than the BE-based cell (263.2 mAh g^{-1} at 0.1 C and 96.5 mAh g^{-1} at 5 C, with a drop of 63.3%, Figure S2

in the Supporting Information). In addition, the BE/T/H-based cell can more efficiently recover its capacity at 0.1 C than the BE-based cell. Compared with BE, the interfacial resistance is significantly reduced in BE/T/H upon electrochemical cycling (Figure S3, Supporting Information), suggesting the existence of Li^+ conductive species at the CEI layer. The better rate performance of BE/T/H suggests the promotion of Li^+ transfer by HTCN + TMSP additives.[43,46] The severe voltage decay is a crucial drawback of LLOs, which has been eliminated by diverse methods such as surface coating and doping.[47,48] As shown in Figure 2d and e, HTCN + TMSP can significantly suppress the voltage decay of the LLO cathode with no prior surface modification. Within 200 cycles, the average discharge voltage decay rate of the BE/T/H-based cell is 0.5 mV/cycle, only half the rate of the BE-based cell (1.0 mV/cycle) (Figure 2e). The outstanding suppression of voltage decay achieved simply by using the low-cost synergistic HTCN + TMSP additives surpasses most reported methods.[49-51] The differential capacity (dQ/dV) curves of the cells using BE and BE/T/H electrolytes are shown in Figure S4 in the Supporting Information. The potential shifts in the BE/T/H case are much smaller than those in the BE case, indicating that HTCN + TMSP can improve the electrochemical reversibility and suppress the voltage decay. Owing to the improved capacity and suppressed voltage decay, the BE/T/H-based cell delivers higher energy densities, with a retention of 91.5% within 200 cycles, compared to the BE-based cell (with a retention of 77.2%) (Figure 2f). Collectively, by combining two additives with different structures and functions, the decomposition of the electrolyte and degradation of the LLO cathode are greatly inhibited by the ion-conductive and protective CEI layer, resulting in high cycling stability, high rate capability, and noticeably slower voltage decay.

2.3. CEI Construction with HTCN + TMSP

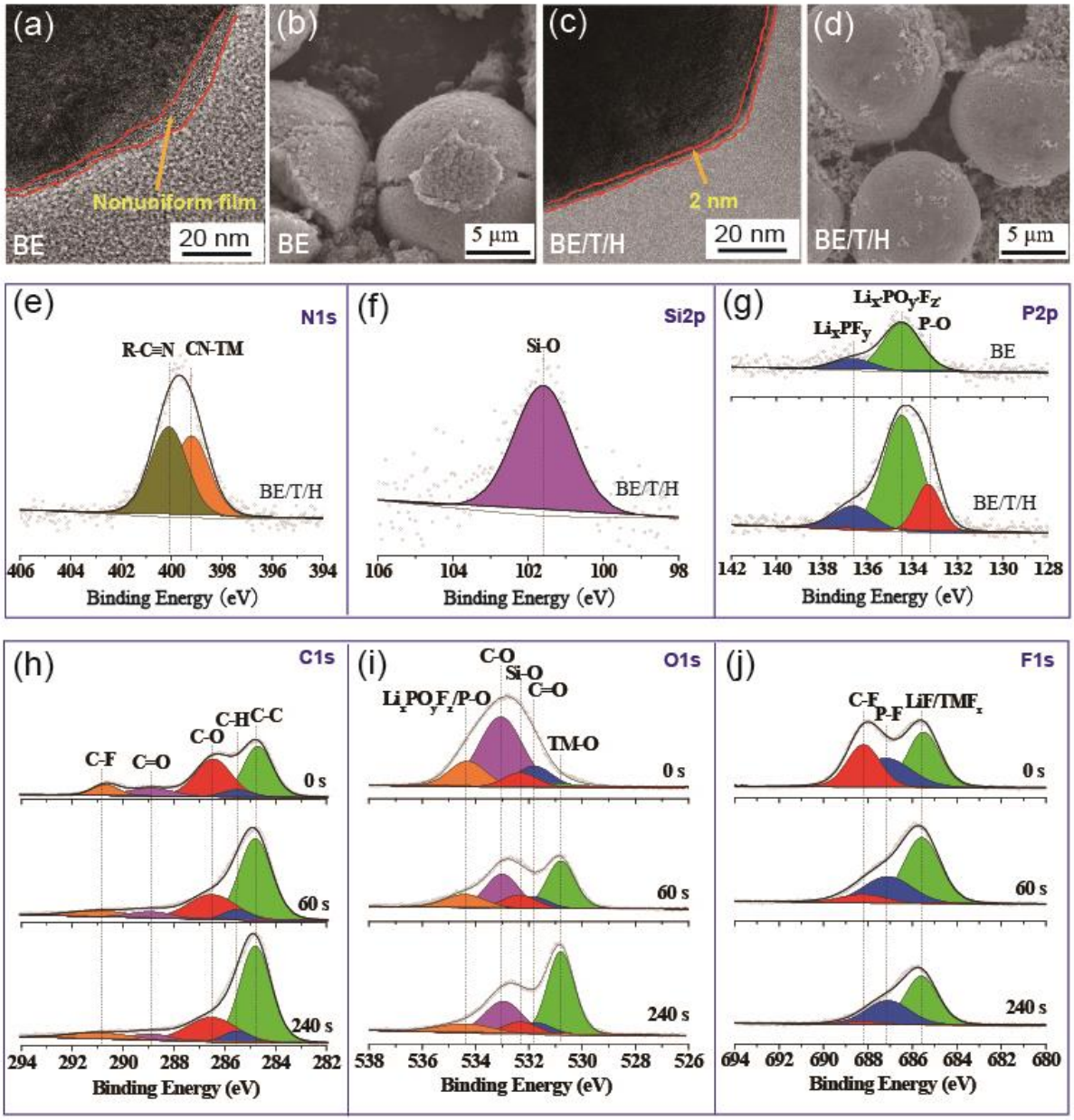

Figure 3. The LLO cathodes and their CEI structures in BE and BE/T/H after 200 cycles at 25 °C. a-d) TEM a, c) and SEM b, d) images of the LLO cycled in BE a, b) and BE/T/H c, d). e-g) XPS N1s e), Si2p f), and P2p g) spectra. h-j) In-depth XPS spectra C1s h), O1s i), and F1s j) of the LLO cycled in BE/T/H sputtered for 0 s, 60 s and 240 s.

To elucidate the effect of CEI chemistry, governed by the synergistic "anchoring + pouring" effect, on the electrochemical performance, the LLO cathodes after cycling in BE and BE/T/H for 200 cycles have been examined by transmission electron microscopy (TEM) and scanning electron microscopy (SEM). As shown in **Figure 3**a and Figure S5a in the Supporting

Information, a thick (up to ~10 nm), nonuniform, and loose CEI layer was formed with BE; this formation is a complicated process correlating with surface corrosion, TM dissolution and irreversible oxygen redox.[10,12] Such a CEI structure cannot effectively protect the LLO from electrolyte contact to avoid further structural degradation and side reactions. As a result, a portion of agglomerated LLO spheres could even severely crack after cycling (Figure 3b and Figure S5b in the Supporting Information). In contrast, the CEI structure formed in BE/T/H is thin (~2 nm), uniform and robust (Figure 3c and Figure S5c in the Supporting Information), and can effectively separate the LLO from the electrolyte to avoid continuous TM dissolution and side reactions. Therefore, the LLO cathode can be efficiently stabilized, as seen from the excellent maintenance of morphology for nearly all agglomerated spheres (Figure 3d and Figure S5d in the Supporting Information).

X-ray photoelectron spectroscopy (XPS) was further used to identify the CEI chemical structures. As shown in the XPS survey spectra in Figure S6a in the Supporting Information, in contrast to BE, BE/T/H leads to the appearance of CEI N1s and Si2p signals, which principally originate from HTCN and TMSP, respectively. In the N1s spectra in Figure 3e, strong CN–TM and R–CN peaks are observable at 399.2 and 400.1 eV, respectively, for the BE/T/H-induced CEI,[35,52] illustrating that HTCN can participate in the CEI construction and coordinate with TM ions. Similarly, owing to the TMSP additive, in Figure 3f, the detectable Si-O signals convincingly demonstrate the participation of TMSP in the formation of CEI. The P-containing species have also been changed by the presence of the additives. As shown in Figure 3g, the cathodes cycled in both BE and BE/T/H contain Li_xPF_y (136.6 eV) and $Li_{x'}PO_{y'}F_{z'}$ (134.5 eV),[53] but these two peaks are significantly stronger than those peaks for BE/T/H. Li_xPF_y and $Li_{x'}PO_{y'}F_{z'}$ can serve as electron insulators to prevent the decomposition of electrolyte solvents, but possess good Li^+ conductivities.[43,54] Besides, compared with the BE-induced CEI, the BE/T/H-induced CEI contains less LiF/TMF_x,[55] as shown by the F1s XPS spectra in Figure

S6b in the Supporting Information. The reduced LiF/TMF_x content means that the deterioration of the LLO surface by the electrolyte has been alleviated.

The chemical structures across the BE/T/H-induced CEI layer were examined by in-depth XPS spectra. The C1s spectrum in Figure 3h indicates the predominant existence of C-C and C-O species and the minor existence of C=O and C-F species. After 60 s of sputtering, the intensities of the C-O and C=O groups are reduced, while the intensity of the C-C group is still large. After 240 s of sputtering, the C-C group becomes more dominant. This trend is further illustrated in the O1s in-depth spectra in Figure 3i. Moreover, the $Li_xPO_yF_z$, content is also reduced after sputtering. On the contrary, as seen from Figure 3j, the LiF/TMF_x content remains high after sputtering, indicating its presence throughout the whole CEI structure. The Si2p and N1s signals also decline upon sputtering, but the N-TM peak can always be deconvoluted (Figure S7, Supporting Information), confirming the coordination between HTCN and TM atoms. The results suggest that HTCN and metal fluorides preferentially construct the inner CEI structure, while the oxidation of solvents predominantly occurs at the outer CEI layer. The as-formed robust and stable CEI structure can effectively protect the LLO from TM dissolution and side reactions, while the small thickness and appropriate composition guarantee fast Li^+ migration across the CEI layer.

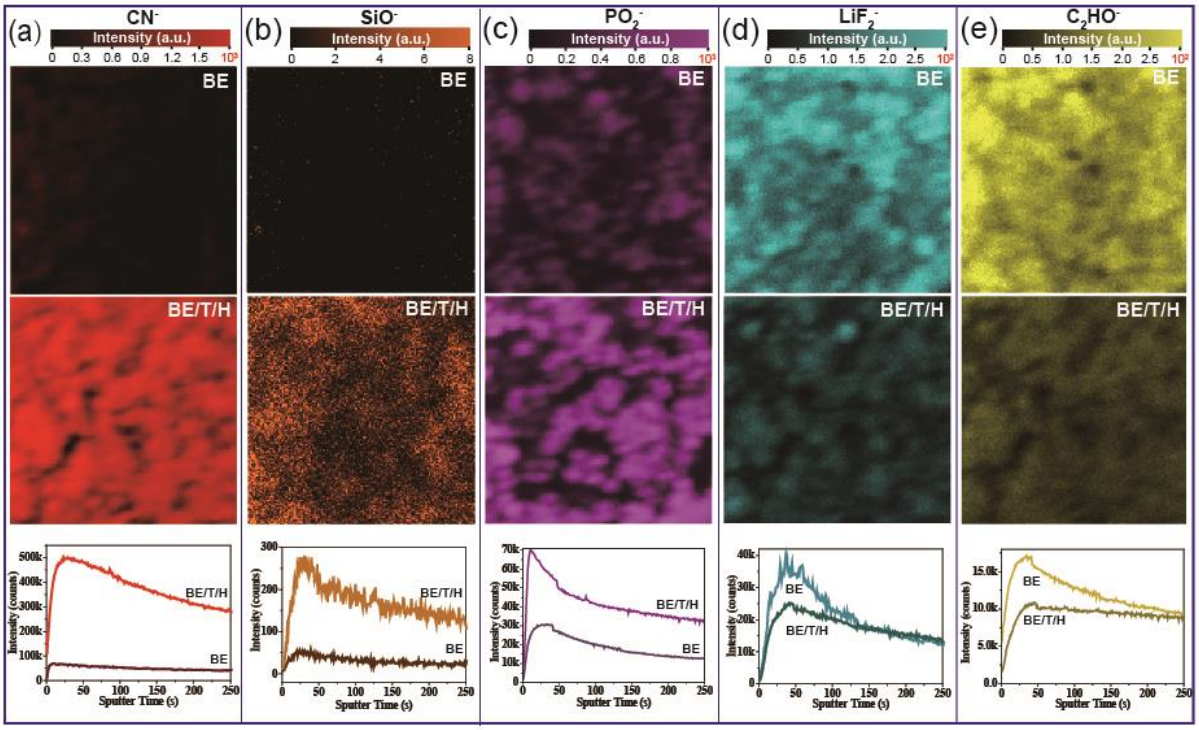

Figure 4. TOF-SIMS investigations of BE- and BE/T/H-induced CEI structures on LLOs after 200 cycles. a) CN^-, b) SiO^-, c) PO_2^-, d) LiF_2^-, and e) C_2HO^- secondary ions. The secondary-ion maps were acquired in a 200 μm × 200 μm TOF-SIMS sputtering region.

In view of its high surface sensitivity and chemical selectivity, time-of-flight secondary ion mass spectrometry (TOF-SIMS) was employed to better elucidate the detailed CEI structures. **Figure 4** shows the secondary ion maps and depth profiles on the surface of the LLOs cycled with BE and BE/T/H (retrieved from half-cells paired with Li anodes after 200 cycles), and the corresponding 3D distributions are displayed in Figure S8 in the Supporting Information. To better illustrate the difference of fragment intensities for the BE- and BE/T/H-based CEI structures, the contrast bars have been set to be nonuniform for some ions. Figure 4a shows that the use of BE/T/H led to much more intense signals from CN^- secondary ions than BE in a 200 μm × 200 μm TOF-SIMS sputtering region. From the in-depth distribution plot in Figure 4a, the CN^- intensity from the BE/T/H-induced CEI is ~7 times larger than that from the BE-induced CEI within the whole sputtering period. This finding strongly demonstrates that HTCN

tends to participate in the construction of the CEI everywhere and across the CEI layer, in good agreement with the XPS results. Similarly, as shown in Figure 4b, the SiO^- signal in the BE/T/H case is more intense than that in the BE case, suggesting the key role of TMSP in forming the BE/T/H-induced CEI layer.

Owing to the participation of TMSP, the P-containing species in the CEI have also been significantly changed. The PO_2^- (Figure 4c), PO^- (Figure S9a, Supporting Information), POF_2^- (Figure S9b, Supporting Information), C_2P^- (Figure S9c, Supporting Information) and P^- (Figure S9d, Supporting Information) secondary ions are much more intense in BE/T/H-induced CEI than in BE-induced CEI. The P-containing species may originate from the decomposition of TMSP and $LiPF_6$. Since the decomposition of $LiPF_6$ was suppressed in BE/T/H (as seen from Figure 4d and discussed below), the more P-containing species obtained when using BE/T/H demonstrates the preferential decomposition of TMSP to construct the CEI layer. In particular, the representative PO_2^- has a very high intensity when BE/T/H is used, suggesting the large portion of PO_2^--related moieties (likely $Li_x{\cdot}PO_y{\cdot}F_z{\cdot}$) in the BE/T/H-induced CEI structure. The PO_2^--related moieties can hinder electron migration but promote Li^+ transfer because of their high ion conductivity and low resistance,[43] and thus the P-rich CEI in the BE/T/H case has the advantages of preventing electrolyte decomposition and improving Li^+ transfer kinetics.

The F-containing species have also been altered by the synergistic additives. Figure 4d shows the 2D distribution and in-depth profile of LiF_2^-, which is predominantly from LiF. Apparently, after adding HTCN and TMSP together, the formation of LiF is significantly reduced, suggesting the suppression of $LiPF_6$ decomposition owing to the synergistic effects of the two additives. Such a suppression effect was further revealed by the reduced contents of F_2^- (Figure S10, Supporting Information), MnF_3^- (Figure S11a, Supporting Information), NiF_3^- (Figure S11b, Supporting Information) and CoF_3^- (Figure S11c, Supporting Information) ions.

Moreover, since TMF_3^- ions most likely originate from the HF corrosion of LLOs, the reduced TMF_3^- in the BE/T/H-induced CEI convincingly prove the suppression of TM dissolution by the synergistic-additive strategy.

In addition, the contents of C_2HO^- (Figure 4e) and $C_2H_3O_2^-$ (Figure S12, Supporting Information) in the BE/T/H-induced CEI are lower than those in the BE-induced CEI, demonstrating the preferential decomposition of EC and DEC at high voltages when no additives are used.[11] The CEI growth can continuously proceed in BE because of the catalytic decomposition of electrolyte upon the reduction of TMs,[56] which is significantly suppressed in BE/T/H. Moreover, continuous CEI growth in BE involves severe competitive deposition/dissolution processes owing to the abundant organic fragments (C_2HO^-, $C_2H_3O_2^-$, etc.), leading to the thick, nonuniform and loose structure noted earlier, which contrasts with the thin, uniform, and robust structure observed with the additives. The fragments detected by TOF-SIMS and its possible effects in BE and BE/T/H are further summarized in Table S2, Supporting Information.

2.4. Mechanism Investigation and Full-cell Performance

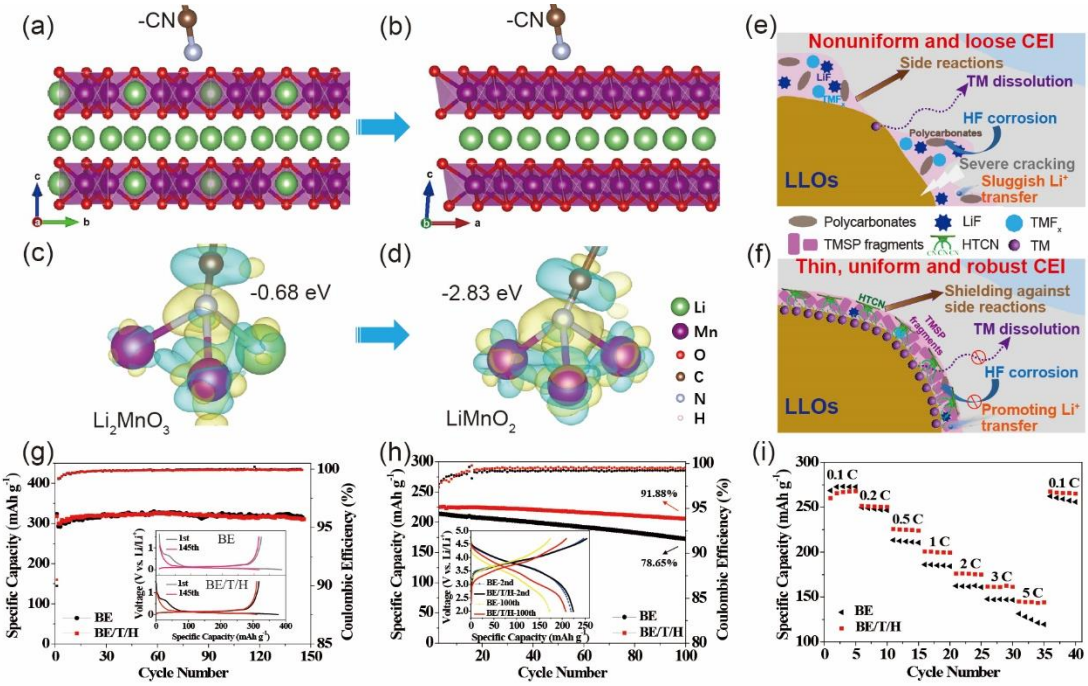

Figure 5. The mechanism of HTCN+TMSP additives and performance of LLOs|Graphite full cells. a, b) The configurations of -CN binding with the Li_2MnO_3 crystal domain in $Li_{1.13}Mn_{0.517}Ni_{0.256}Co_{0.097}O_2$ upon the electrochemical evolution from the pristine a) to the monoclinic manganese-based $LiTMO_2$ structure b). c, d) The differential charge densities of -CN binding with the pristine Li_2MnO_3 crystal domain c) and the evolved monoclinic manganese-based $LiTMO_2$ structure d). The yellow and blue regions indicate electron increase and decrease, respectively. The value for the isosurface is 0.003 e $Bohr^{-3}$. e, f) Schematic illustrations of the mechanism of BE-induced e) and BE/T/H-induced f) CEI on LLOs. g) The cycle performance of Li|graphite half-cells using BE and BE/T/H electrolytes at 72 mAh g^{-1}, and (inset) the charge-discharge curves. h, i) Electrochemical performance of $Li_{1.13}Mn_{0.517}Ni_{0.256}Co_{0.097}O_2$|graphite full cells using BE and BE/T/H electrolytes: cycle performance h) (inset is charge-discharge curves of 2nd and 100th cycles), and rate performance i) at 0.5 C and 25 ℃.

The anchoring effect of HTCN nitrile groups on surface TM (mostly Mn) atoms is one of the key advantages of the modified electrolyte, which has not been well understood so far. Therefore, a more explicit picture of the anchoring effect of HTCN was theoretically developed. It should be noted that such an anchoring effect should be considered in the context of an electrochemically dynamic process involving LLOs rather than static states. During the initial cycle, LLOs with "twin domains" of monoclinic Li_2MnO_3 and rhombohedral $LiTMO_2$ structures can transform into a "core-shell" structure,[7] and the bulk structure is dominated by the monoclinic $LiTMO_2$ structure because of the lattice densification process. Therefore, the binding behaviors of HTCN to the (001) surfaces of Li_2MnO_3 and $LiMnO_2$ (representing structures in the pristine state and the evaluated state after the initial cycle, respectively) were computed, as displayed in **Figure 5**a-d. The rational binding configuration of -CN with Li_2MnO_3 (or formularized as $Li(LiMn_2)_{1/3}O_2$ possessing a $LiMn_2$ layer) allows two-Mn coordination (Figure 5a and Figure S13 in the Supporting Information), while that with $LiMnO_2$ (possessing a TM layer) allows three-Mn coordination (Figure 5b). For both Li_2MnO_3 and $LiMnO_2$, the differential charge density shows the electron accumulation in the region between N and Mn, while the electron density around the C in -CN decreases, indicating the electron

donation from -CN to Mn (Figure 5c, d). The binding energy of HTCN on $LiMnO_2$ was calculated to be −2.83 eV, significantly larger than that of Li_2MnO_3 (−0.68 eV). Note here that only one -CN group was involved in the calculation, which means that the calculated binding energies are largely underestimated. Therefore, HTCN can tightly anchor the LLO owing to the strong coordination between the -CN and $LiTMO_2$ structures; such an anchoring effort is further strengthened during the electrochemical cycling by the transformation from the Li_2MnO_3 to the $LiTMO_2$ structure. Moreover, the contents of Mn, Co and Ni adsorbed on the Li anodes and separators dissolved from cycled cathodes have been examined by inductively coupled plasma-atomic emission spectrometer (ICP-AES) (Figure S14, Supporting Information), which clearly show that all the dissolved transition metals become less when HTCN was used. The effective suppression of TM dissolution and the accompanying irreversible surface rearrangement is thus theoretically and experimentally illustrated.

On the basis of the above studies, the mechanism by which synergistic HTCN + TMSP electrolyte additives modify the electrolyte and enhance the electrochemical performance of the LLO is proposed as schematically illustrated in Figure 5e, f. BE alone, as an electrolyte for LLOs, has several key drawbacks, including (1) the incompatibility with high voltage, (2) the promotion of TM dissolution and accompanying LLO structural degradation, and (3) the severe side reactions ($LiPF_6$ decomposition with HF release, solvent oxidation, irreversible oxygen redox, etc.), as partially reflected by the thick, nonuniform and loose CEI layer (Figure 5e). These drawbacks can be effectively addressed by using the synergistic HTCN + TMSP electrolyte additives to construct *in situ* a thin, uniform and robust CEI layer, a complicated process involving the dominant participation of both HTCN and TMSP (Figure 5f). HTCN tightly anchors to the LLO surface without decomposition even at high voltages, playing a "steel bar-like" anchoring role in the CEI formation. In contrast, TMSP serves as an oxidative sacrificer, playing a cement-like role by triggering the pouring together of diverse fragments to

construct the CEI layer. Such an "anchoring + pouring" synergy endows the CEI layer with promising physical properties (thickness, uniformity, and robustness) and chemical composition, which can compensate for the major drawbacks of BE, as follows: (1) The derived CEI layer prevents direct contact between the LLO and solvents, thereby raising the onset oxidation potential of the electrolyte to realize high-voltage feasibility. HTCN has pronounced anti-oxidation properties, further stabilizing the electrolyte at high voltages. (2) As suggested by the experimental investigations and theoretical calculations, HTCN can stabilize $LiTMO_2$ and Li_2MnO_3 (especially when electrochemically converted to an monoclinic $LiTMO_2$ structure) at the LLO surface through the coordination between -CN and TMs. Therefore, TM dissolution can be effectively suppressed, reducing the LLO surface degradation. (3) The thin, uniform, and robust CEI layer can effectively shield the LLO against diverse side reactions, such as solvent oxidation, $LiPF_6$ decomposition, and irreversible oxygen redox. The CN-, P- and Si-enriched CEI layer is also Li^+-conductive to favor efficient Li^+ transfer, while its small thickness cannot greatly impede the Li^+ diffusion. With the collective benefits of high-voltage feasibility, suppressed TM dissolution, and alleviated side reactions, the synergistic HTCN + TMSP electrolyte additives significantly improve the electrochemical cycling stability, rate capacity, and discharge voltage maintenance of LLOs.

To evaluate the effectiveness of our synergistic-additive strategy in practical LIBs, the modified BE/T/H was further used in $Li_{1.13}Mn_{0.517}Ni_{0.256}Co_{0.097}O_2$|graphite full cells. First, the influences of TMSP + HTCN on the Li|graphite half-cell were examined. It was found that both the BE/T/H-based and BE-based Li|graphite half-cells display similar initial charge/discharge curves, charge capacities and capacity retentions (Figure 5g), suggesting that the compatibility of HTCN + TMSP modified electrolyte with the graphite anode is comparable to that of the commercial $LiPF_6$ in EC/DEC electrolyte, in agreement with the LUMOs of the electrolyte components (Figure 1b). For the full cells, as shown in Figure 5h, the modified BE/T/H yields

an initial capacity of 224.1 mAh g^{-1}, a capacity retention of 91.88% within 100 cycles, and an average Coulombic efficiency of 99.26%, while BE only yields an initial capacity of 219.2 mAh g^{-1}, a capacity retention of 78.65%, and a Coulombic efficiency of 99.01%. The LUMO level of TMSP is slightly lower than that of EC and DEC, suggesting that TMSP can participate in the formation of SEI to a certain extent and reduce the destructive effect of solvated lithium ions on the graphite anode structure. However, such effect should not be very strong. Moreover, the BE/T/H-based full cell has a better rate capability than the BE-based full cell (Figure 5i), highlighting the promotion of electrochemical reaction kinetics by the synergistic HTCN + TMSP additives. The performance enhancement of the BE/T/H-based full cell demonstrates the versatility of the synergistic-additive strategy for practical batteries.

3. Conclusion

In conclusion, an *in situ* "anchoring + pouring" CEI construction strategy has been proposed to modify an LLO cathode to enhanced the electrochemical stability. HTCN has high anti-oxidation ability and strongly coordinates with TMs (mostly Mn) at the LLO surface, while TMSP serves as an oxidative sacrificer at high voltages. The cycle stability and rate capacity of the LLO cathode without pre-modification has been greatly enhanced, and the severe discharge-voltage decay has been reduced to a noticeable low level of 0.50 mV/cycle. During electrochemical cycling, HTCN anchors on the LLO surface as a CEI framework and TMSP facilitates the pouring of diverse moieties, thereby *in situ* constructing a CEI layer through the "anchoring + pouring" synergy. This construction endows the CEI layer with promising physical properties (~2-nm thickness, uniformity, and robustness) and appropriate chemical composition (-CN, P, and Si-rich), as identified by a series of analytical methods, especially TOF-SIMS; these properties and composition noticeably improve the high-voltage stability of the electrolyte, suppress TM (mostly Mn) dissolution, and shield against diverse electrochemical side reactions. The key anchoring effect of HTCN has been theoretically

demonstrated by its strong coordination with $LiMnO_2$, which can be further strengthened during the electrochemical evolution process of Li_2MnO_3 crystal domains in LLOs. Considering the effectiveness, convenience and low cost of synergistic additives as well as their compatibility with graphite anodes, the proposed strategy paves a new avenue to overcome the intrinsic challenges of LLOs toward practical, high-energy and long-life LIBs.

4. Experimental Section

Fabrication of Electrodes: The cathode was prepared by mixing slurries of 80 wt.% active $Li_{1.13}Mn_{0.517}Ni_{0.256}Co_{0.097}O_2$ material, 10 wt.% acetylene black, and 10 wt.% poly-vinylidene difluoride (PVDF, dissolved in N-methyl-2-pyrrolidone) on Al foil, and then dried for 8 hours in a vacuum oven at 100 °C. $Li_{1.13}Mn_{0.517}Ni_{0.256}Co_{0.097}O_2$|Li half-cells were assembled with Celgard-2400 as separator and Li foil as the anode. The graphite electrode was prepared by coating Cu foil with slurries of graphite, super P and PVDF with a weight ratio of 80:10:10. Li|graphite half-cells used Li foil as the counter electrode. Finally, coin-type $Li_{1.13}Mn_{0.517}Ni_{0.256}Co_{0.097}O_2$|graphite full cells were constructed with different electrolytes. The reversible negative-to-positive capacity ratio was about 1.12, based on the capacities of 260 mA h g^{-1} for $Li_{1.13}Mn_{0.517}Ni_{0.256}Co_{0.097}O_2$ and 320 mA h g^{-1} for graphite.

Electrolyte Preparation: The 1 M $LiPF_6$ dissolved in EC/DEC (1:1 by volume) was used as the baseline electrolyte (BE). The BE/T, BE/H, and BE/T/H electrolytes were prepared by adding 1 wt.% TMSP, 1 wt.% HTCN, and 0.5 wt.% TMSP + 0.5 wt.% HTCN, respectively.

Electrochemical Testing and Characterization: Electrochemical tests were carried out with CR2032 coin cells. The electrochemical performance was tested on a LAND CT2001C battery tester at 25 °C with different current densities. The $Li_{1.13}Mn_{0.517}Ni_{0.256}Co_{0.097}O_2$|Li cells were cycled between 2.0 and 4.8 V at 0.1 C (1 C = 200 mA g^{-1}) during the first cycle, and then between 2.0 and 4.6 V at 1 C. The Li|graphite cells were initially activated at 0.1 C and then cycled at 0.2 C between 0.001 and 1.5 V. The $Li_{1.13}Mn_{0.517}Ni_{0.256}Co_{0.097}O_2$|graphite full cells

were activated between 2 and 4.75 V at 0.1 C, and then tested between 2 and 4.7 V at 0.5 C in the following cycles.

Linear sweep voltammetry (LSV) and electrochemical impedance spectroscopy (EIS) tests were performed on a Solartron Analytical Instrument at 25 °C. The electrochemical window was tested with a two-electrode system, in which stainless steel sheet was used as the working electrode, and Li sheet was used as the counter and reference electrodes. The voltage range was 3–6 V, and the scanning speed was 0.1 mV s^{-1}. The EIS was measured with an AC voltage of 5 mV amplitude, and the frequency range was from 10^5 Hz to 10^{-2} Hz. The cycled $Li_{1.13}Mn_{0.517}Ni_{0.256}Co_{0.097}O_2$ electrodes were carefully dismantled from the completely discharged cells and subsequently rinsed with DMC solvent to remove residues, and then dried under vacuum at room temperature for 8 h before analysis.

The morphologies of cycled $Li_{1.13}Mn_{0.517}Ni_{0.256}Co_{0.097}O_2$ electrodes were investigated by Hitachi field-emission SEM (FE-SEM, S-4800) and TEM (FEI Titan TM G2 80-200, 300 kV). The ^{19}F NMR spectrum was acquired from a 400 MHz Bruker NMR spectroscopy instrument (ASCEndTM400 [AVANCE HD III], Germany). The stabilizing effects of TMSP and HTCN on H_2O and HF removal after the storage of electrolytes for 24 h were investigated. When adding additives, deionized water (0.1 vol.%) was added to electrolytes to evaluate the reactivity of additives to H_2O and HF. An inner NMR tube containing chloroform-d ($CDCl_3$) was used as the reference. When performing XPS (PHI Quanteral II, Japan, with an Al K = 280.00 eV excitation source), the binding energies were calibrated according to the peak of 284.8 eV in the C1s spectrum to reduce the charge effect. TOF-SIMS analysis was performed with a TOF-SIMS 5-100 spectrometer (ION-TOF GmbH). All detected secondary ions of interest have a mass range of 0–900 aum and possess negative polarity. The pulsed 30-keV Bi_1^+ ion beam in a high-current mode was used for depth profiling and 1000-eV Cs^+ was used as the sputtering ion beam in a typical sputtered area (200 μm × 200 μm). With the XPS and TOF-SIMS measurements, all samples were transferred from an argon-filled glove box to the

instrument to ensure as little exposure as possible to the air. The dissolution of the transition metal ions was measured by inductively coupled plasma-atomic emission spectrometer (ICP-AES, OPTIMA7000DV). The cycled separators and lithium electrode for ICP analyses were rinsed three times with DMC solvent and dissolved in 10 mL 2% HNO_3.

Computation Methods: To calculate the adsorption energies, the Vienna Ab initio Simulation Package (VASP) was used with the projector augmented wave method for the description of electron-core interactions.[57,58] The energy cutoff of the plane-wave basis set is 500 eV. To account for the energy of localized 3d orbitals of TM atoms, we adopted PBE + U as the exchange-correlation function, where the U-J values for the 3d orbitals of Mn, Co, and Ni were set as 3.9, 3.32 and 6.2 eV, respectively.[59-61] The DFT-D3 method was used for a better evaluation of van der Waals interactions, which are crucial for the adsorption energy and structure.[62,63] The first Brillouin zone was sampled in a Gamma-centered mesh with one k-point. The surface model of the $LiTMO_2$ (TM=Mn, Co or Ni) (001) face is composed of 50 $LiTMO_2$ units, and the Li_2MnO_3 (001) face is composed of 36 Li_2MnO_3 units. The bottom halves of the atoms in all the surface models were fixed in the structural relaxation. The differential charge density (ρ_{diff}) was calculated as

$$\rho_{diff} = \rho_{HTCN-surf} - \rho_{HTCN} - \rho_{surf} \qquad (1)$$

where ρ_{HTCN}, ρ_{surf} and $\rho_{HTCN-surf}$ stand for the charge density of the HTCN molecule, the cathode surface, and the surface with HTCN binding, respectively. The bulk structures, surface structures and differential charge density were plotted with VESTA.[64]

The geometric optimization and HOMO/LUMO computation of HTCN, EC, DEC, TMSP, and PF_6^- molecules/ions were performed using the Gaussian 09 quantum chemistry package with the B3LYP hybrid functional.[65-67] The optimization was performed with a 6-31G(d) basis set, while the electronic structures were calculated at the 6-311G + (d, p) level. The polarizable continuum model was adopted to implicitly evaluate the EC/DEC solvent effects.

Supporting Information

Supporting Information is available from the Wiley Online Library or from the author.

Acknowledgements

J. Z., Y. L. and X. Z. contributed equally to this work. This work was financially supported by the Beijing Natural Science Foundation (JQ19003), National Natural Science Foundation of China (Grants 21975006, 21875007, 51802009 and U19A2018), the National Key R&D Program of China (Grant No. 2018YFB0104302), Project of Youth Talent Plan of Beijing Municipal Education Commission (CIT&TCD201804013) and Beijing Natural Science Foundation (KZ201910005002, KZ202010005007 and L182009). K. Amine gratefully acknowledge support from Clean Vehicles, US-China Clean Energy Research Centre (CERC-CVC2).

Received: ((will be filled in by the editorial staff))
Revised: ((will be filled in by the editorial staff))
Published online: ((will be filled in by the editorial staff))

References

[1] Z. P. Cano, D. Banham, S. Y. Ye, A. Hintennach, J. Lu, M. Fowler, Z. W. Chen, *Nature Energy* **2018**, *3*, 279.

[2] R. Schmuch, R. Wagner, G. Hörpel, T. Placke, M. Winter, *Nature Energy* **2018**, *3*, 267.

[3] X. Q. Zeng, M. Li, D. A. El-Hady, W. Alshitari, A. S. Al-Bogami, J. Lu, K. Amine, *Adv. Energy Mater.* **2019**, *9*,1900161.

[4] W. D. Li, B. H. Song, A. Manthiram, *Chem. Soc. Rev.* **2017**, *46*, 3006.

[5] H. J. Yu, H. S. Zhou, *J. Phys. Chem. Lett.* **2013**, *4*, 1268.

[6] N. Yabuuchi, K. Yoshii, S.-T. Myung, I. Nakai, S. Komaba, *J. Am. Chem. Soc.* **2011**, 133, 4404.

[7] H. J. Yu, Y.-G. So, Y. Ren, T. H. Wu, G. C. Guo, R. J. Xiao, J. Lu, H. Li, Y. B. Yang, H. S. Zhou, R. Z. Wang, K. Amine, Y. Ikuhara, *J. Am. Chem. Soc.* **2018**, *140*, 15279.

[8] K. Zhang, B. Li, Y. X. Zuo, J. Song, H. F. Shang, F. H. Ning, D. G. Xia, *Electrochemical Energy Reviews*

2019, *2*, 606.

[9] P. F. Yan, A. Nie, J. M. Zheng, Y. G. Zhou, D. P. Lu, X. F. Zhang, R. Xu, I. Belharouak, X. T. Zu, J. Xiao, K. Amine, J. Liu, F. Gao, R. Shahbazian-Yassar, J. G. Zhang, C. M Wang, *Nano Lett.* **2015**, *15*, 514.

[10] J. Xu, M. L. Sun, R. M Qiao, S. E. Renfrew, L. Ma, T. P. Wu, S. Hwang, D. Nordlund, D. Su, K. Amine, J. Lu, B. D. McCloskey, W.L. Yang, W. Tong, *Nat. Commun.* **2018**, *9*, 947.

[11] Q. H. Li, Y. Wang, X. L. Wang, X. R. Sun, J. N. Zhang, X. Q. Yu, H. Li, *ACS Appl Mater Interfaces* **2020**, *12*, 2319.

[12] C. Zhan, T. P. Wu, J. Lu, K. Amine, *Energy & Environ. Sci.* **2018**, *11*, 243.

[13] E. M. Erickson, W. D. Li, A. Dolocan, A. Manthiram, *ACS Appl. Mater. Interfaces* **2020**, *12*, 16451.

[14] Y. Li, M. Bettge, B. Polzin, Y. Zhu, M. Balasubramanian, D. P. Abraham, *J. Electrochem. Soc.* **2013**, *160*, A3006.

[15] H. Gao, J. Y. Cai, G.-L. Xu, L. X. Li, Y. Ren, X. B. Meng, K. Amine, Z. H. Chen, *Chem. Mater.* **2019**, *31*, 2723.

[16] S.-Q. Yang, P.-B. Wang, H.-X. Wei, L.-B. Tang, X.-H. Zhang, Z.-J. He, Y.-J. Li, H. Tong, J.-C. Zheng, *Nano Energy* **2019**, *63*, 2211.

[17] A. M. Haregewoin, A. S. Wotango, B.-J. Hwang, *Energy Environ. Sci.* **2016**, *9*, 1955.

[18] H. J. Zhao, X. Q. Yu, J. D. Li, B. Li, H. Y. Shao, L. Li, Y. H. Deng, *J. Mater. Chem. A.* **2019**, *7*, 8700.

[19] N.-S. Choi, J.-G. Han, S.-Y. Ha, I. Park, C.-K. Back, *RSC Advances* **2015**, *5*, 2732.

[20] W. M. Zhao, Y. J. Ji, Z. R. Zhang, M. Lin, Z. L. Wu, X. Zheng, Q. Li, Y. Yang, *Current Opinion in Electrochemistry* **2017**, *6*, 84.

[21] J. H. Li, Z. S Wang, *J. Power Sources* **2020**, *450*, 227648.

[22] Y. M. Meng, G. R. Chen, L. Y. Shi, H. J. Liu, D. S. Zhang, *ACS Appl. Mater. Interfaces* **2019**, *11*, 45108.

[23] M. Hekmatfar, A. Kazzazi, G. G. Eshetu, I. Hasa, S. Passerini, *ACS Appl. Mater. Interfaces* **2019**, *11*, 43166.

[24] C. Yan, R. Xu, Y. Xiao, J.-F. Ding, L. Xu, B.-Q. Li, J.-Q. Huang, *Adv. Functional Mater.* **2020**, *30*, 1909887.

[25] Z. Xiao, J. D. Liu, G. L. Fan, M. Yu, J. X. Liu, X. L. Gou, M. J. Yuan, F. Y. Cheng, *Mater. Chem. Front.* **2020**, *4*, 1689.

[26] J. H. Li, Y. Q. Liao, W. Z. Fan, Z. F. Li, G. J. Li, Q. K. Zhang, L. D. Xing, M. Q. Xu, W. S. Li, *ACS Appl.Energy Mater.* **2020**, *3*, 3049.

[27] C. C. Ye, W. Q. Tu, L. M. Yin, Q. F. Zheng, C. Wang, Y. T. Zhong, Y. G. Zhang, Q. M. Huang, K. Xu, W. S. Li, *J. Mater. Chem. A* **2018**, *6*, 17642.

[28] M. S. Park, Y. S. Kang, D. Im, S. G. Doo, H. Chang, *Phys. Chem. Chem. Phys.* **2014**, *16*, 22391.

[29] T. Evans, D. M. Piper, H. X. Sun, T. Porcelli, S. C. Kim, S. S. Han, Y. S. Choi, C. X. Tian, D. Nordlund, M. M. Doeff, C. M. Ban, S. J. Cho, K. H. Oh, S. H. Lee, *Adv. Mater.* **2017**, *29*, 1604549.

[30] H. J. Yu, R. Ishikawa, Y.-Gi. So, N. Shibata, T. Kudo, H. S. Zhou, Y. Ikuhara, *Angew. Chem. Int. Ed.* **2013**, *52*, 5969.

[31] H. J. Yu, Y.-G. So, A. Kuwabara, E. Tochigi, N. Shibata, T. Kudo, H. S. Zhou, Y. Ikuhara, *Nano Lett.* **2016**, *16*, 2907.

[32] T. H. Wu, X. Liu, X. Zhang, Y. Lu, B. Y. Wang, Q. S. Deng, Y. B. Yang, E. R. Wang, Z. T. Lyu, Y. Q. Li, Y. T. Wang, Y. Lyu, C. F. He, Y. Ren, G. L. Xu, X. L. Sun, K. Amine, H. J. Yu, *Adv. Mater.***2020**, 2001358.

[33] E. R. Wang, Y. Zhao, D. D. Xiao, X. Zhang, T. H. Wu, B. Y. Wang, M. Zubair, Y. Q. Li, X. L. Sun, H. J. Yu, *Adv. Mater.***2020**, 1906070.

[34] H. Z. Zhi, L. D. Xing, X. W. Zheng, K. Xu, W. S. Li, *J. Phys. Chem. Lett.* **2017**, *8*, 6048.

[35] Y.-S. Kim, H. Lee, H.-K. Song, *ACS Appl. Mater. Interfaces* **2014**, *6*, 8913.

[36] Y. J. Ji, Z. R. Zhang, M. Gao, Y. Li, M. J. McDonald, Y. Yang, *J. Electrochem. Soc.* **2015**, *162*, A774.

[37] B. Liao, X. L. Hu, M. Q. Xu, H. Y. Li, L. Yu, W. Z. Fan, L. D. Xing, Y. H. Liao, W. S. Li, *J. Phys. Chem. Lett.* **2018**, *9*, 3434.

[38] R. Xu, X.-B. Cheng, C.Yan, X.-Q. Zhang, Y. Xiao, C.-Z. Zhao, J.-Q. Huang, Q. Zhang, *Matter* **2019**, *1(2)*, 317.

[39] X. L. Liao, X. W. Zheng, J. W. Chen, Z. Y. Huang, M. Q. Xu, L. D. Xing, Y. H. Liao, Q. L. Lu, X. F. Li, W. S. Li, *Electrochimica Acta* **2016**, *212*, 352.

[40] C. Bolli, A. Guéguen, M. A. Mendez, E. J. Berg, *Chem. Mater.* **2019**, *31*, 1258.

[41] R. J. Chen, F. Liu, Y. Chen, Y. S. Ye, Y. X. Huang, F. Wu, L. Li, *J. Power Sources* **2016**, *306*, 70.

[42] J.-G. Han, M.-Y. Jeong, K. Kim, C. Park, C. H. Sung, D. W. Bak, K. H. Kim, K.-M. Jeong, N.- S. Choi, *J. Power Sources* **2019**, *446*, 227366.

[43] K. Xu, *Chem. Rev.* **2014**, *114*, 11503.

[44] J. W. Chen, L. D. Xing, X. R. Yang, X. Liu, T. J. Li, W. S.Li, *Electrochimica Acta* **2018**, *290*, 568.

[45] K. Kim, D. Hwang, S. Kim, S. O Park, H. Cha, Y.-S. Lee, J. Cho, S. K. Kwak, N.-S. Choi, *Adv. Energy Mater.* **2020**, *10*, 2000012.

[46] S. S. Zhang, *InfoMat.* **2019**, *2*, 942.

[47] W. Zhang, Y. G. Sun, H. Q. Deng, J. M. Ma, Y. Zeng, Z. Q. Zhu, Z. S. Lv, H. Xia, X. Ge, S. K. Cao, Y. Xiao, S. B. Xi, Y. h. Du, A. M. Cao, X. D. Chen, *Adv. Mater.* **2020**, *32*, e2000496.

[48] P. K. Nayak, J. Grinblat, M. Levi, E. Levi, S. Kim, J. W. Choi, D. Aurbach, *Adv. Energy Mater.* **2016**, *6*, 1502398.

[49] X. K. Ding, D. Luo, J. x. Cui, H. X. Xie, Q. Q. Ren, Z. Lin, *Angew. Chem. Int. Ed.* **2020**, *59*, 7778.

[50] S. Liu, Z. P. Liu, X. Shen, W. H. Li, Y. R. Gao, M. N. Banis, M. Li, K. Chen, L. Zhu, R. C. Yu, Z. X. Wang, X. L. Sun, G. Lu, Q, Y. Kong, X. D. Bai, L. Q. Chen, *Adv. Energy Mater.* **2018**, *8*, 1802105.

[51] J. S. Yang, P. Li, F. P. Zhong, X. M. Feng, W. H Chen, X. P. Ai, H, X. Yang, D. G. Xia, Y. L. Cao, *Adv. Energy Mater.* **2020**, *10*, 1904264.

[52] A. Nurpeissova, D.-I. Park, S.-S. Kim, Y.-K. Sun, *J. Electrochem. Soc.* **2015**, *163*, A171.

[53] G. J. Xu, C. G. Pang, B. B. Chen, J. Ma, X. Wang, J. C. Chai, Q. F. Wang, W. Z. An, X. H Zhou, G. L. Cui, L. Q. Chen, *Adv. Energy Mater.* **2018**, *8*, 1701398.

[54] X.-Y. Yue, W.-W. Wang, Q.-C. Wang, J.-K. Meng, X. X. Wang, Y. Song, Z.-W.Fu, X.-J. Wu, Y.-N. Zhou, *Energy Storage Materials* **2019**, *21*, 180.

[55] C. Wang, L. D. Xing, J. Vatamanu, Z. Chen, G. Y. Lan, W. S. Li, K. Xu, *Nat Commun.* **2019**, *10*, 3423.

[56] J. Y. Li, W. D. Li, Y. You, A. Manthiram, *Adv. Energy Mater.* **2018**, *8*, 1801957.

[57] G. Kresse, J. Furthmüller, *Phys. Rev. B.* **1996**, *54*, 11169.

[58] G. Kresse, D. Joubert, *Phys. Rev. B.* **1999**, *59*, 1758.

[59] J. P. Perdew, K. Burke, M. Ernzerhof, *Phys. Rev. Lett.* **1996**, *77*, 3865.

[60] V. I. Anisimov, F. Aryasetiawan, A. I. Lichtenstein, *J. Phys.: Condens. Matter* **1997**, *9*, 767.

[61] V. I. Anisimov, J. Zaanen, O. K. Andersen, *Phys. Rev. B.* **1991**, *44*, 943.

[62] S. Grimme, J. Antony, S. Ehrlich, H. Krieg, *J. Chem. Phys.* **2010**, *132*, 154104.

[63] S. Grimme, S. Ehrlich, L. Goerigk, *J. Comput. Chem.* **2011**, *32*, 1456.

[64] K. Momma, F. Izumi, J. Appl. Cryst. **2011**, *44*, 1272.

[65] Frisch, M. J. et al. Gaussian 09, Revision E.01 **2009**.

[66] A. D. Becke, *J. Chem. Phys.* **1993**, *98*, 5648.

[67] C. Lee, W. Yang, R. G. Parr, *Phys. Rev. B.* **1988**, *37*, 785.